POLITECNICO DI TORINO
Repository ISTITUZIONALE

Controlling Domain-Wall Nucleation in Ta/Co-Fe-B/MgO Nanomagnets via Local Ga+ Ion Irradiation

Original
Controlling Domain-Wall Nucleation in Ta/Co-Fe-B/MgO Nanomagnets via Local Ga+ Ion Irradiation / Mendisch, S., Riente, F., Ahrens, V., Gnoli, L., Haider, M., Opel, M., Kiechle, M., Ruo Roch, M., Becherer, M.. - In: PHYSICAL REVIEW APPLIED. - ISSN 2331-7019. - ELETTRONICO. - 16:1(2021). [10.1103/PhysRevApplied.16.014039]

Availability:
This version is available at: 11583/2913594 since: 2021-07-19T08:46:37Z

Publisher:
American Physical Society

Published
DOI:10.1103/PhysRevApplied.16.014039

Terms of use:

This article is made available under terms and conditions as specified in the corresponding bibliographic description in the repository

Publisher copyright
GENERICO -- per es. Nature : semplice rinvio dal preprint/submitted, o postprint/AAM [ex default]

The original publication is available at https://journals.aps.org/prapplied/abstract/10.1103/PhysRevApplied.16.014039 / http://dx.doi.org/10.1103/PhysRevApplied.16.014039.

(Article begins on next page)

10 October 2026

Controlling Domain-Wall Nucleation in Ta/Co-Fe-B/MgO Nanomagnets via Local Ga^+ Ion Irradiation

Simon Mendisch,[1,*] Fabrizio Riente,[2,†] Valentin Ahrens,[1] Luca Gnoli,[2] Michael Haider,[1] Matthias Opel,[3] Martina Kiechle,[1] Massimo Ruo Roch,[2] and Markus Becherer[1]

[1] *Department of Electrical and Computer Engineering, Technical University of Munich, Arcisstraße 21, Munich 80333, Germany*

[2] *Department of Electronics and Telecommunications Engineering, Politecnico di Torino, Turin 10129, Italy*

[3] *Bavarian Academy of Sciences, Walther-Meißner-Straße 8, Garching 85748, Germany*

(Received 16 February 2021; revised 8 May 2021; accepted 1 June 2021; published 15 July 2021)

Comprehensive control of the domain-wall nucleation process is crucial for spin-based emerging technologies ranging from random-access and storage-class memories through domain-wall logic concepts to nanomagnetic logic. In this work, focused Ga^+ ion irradiation is investigated as an effective means to control domain-wall nucleation in Ta/Co-Fe-B/MgO nanostructures. We show that, analogously to He^+ irradiation, it is not only possible to reduce the perpendicular magnetic anisotropy but also to increase it significantly, enabling bidirectional manipulation schemes. First, the irradiation effects are assessed at the film level, sketching an overview of the dose-dependent changes in the magnetic energy landscape. Subsequent time-domain nucleation characteristics of irradiated nanostructures reveal substantial increases in the anisotropy fields but surprisingly small effects on the measured energy barriers, indicating shrinking nucleation volumes. Spatial control of the domain-wall nucleation point is achieved by employing focused irradiation of preirradiated magnets, with the diameter of the introduced circular defect controlling the coercivity. Special attention is given to the nucleation mechanisms, changing from the coherent radiation of a Stoner-Wohlfarth particle to depinning from an anisotropy gradient. Dynamic micromagnetic simulations and related measurements are used in addition to model and analyze this depinning-dominated magnetization reversal.

DOI: 10.1103/PhysRevApplied.16.014039

I. INTRODUCTION

Magnetic nanostructures based on cobalt-iron-boron–magnesium-oxide (Co-Fe-B/MgO) thin films, with and without perpendicular magnetic anisotropy (PMA), play a vital role in many emerging technologies, from magnetic-tunnel-junction-based sensors through nonvolatile storage technologies, to domain-wall and nanomagnetic logic applications [1–5]. In particular, logic applications necessitate precise control of the magnetic energy landscape to nucleate, propagate, and pin or depin domain walls—a level of control that remains a significant challenge [6,7]. As a widely established semiconductor technology with unmatched spatial resolution and a wide tuning range, ion irradiation is ideally suited to address these issues [8]. It offers a realistic perspective to modify magnetic properties with nanometer precision. So far, studies on the irradiation effects on Co-Fe-B/MgO have mainly been restricted to film-level investigations and light (He^+) ions [9–11]. In this work, we investigate the usage of heavier Ga^+ ions in an attempt to create artificial nucleation centers (ANCs) in Ta/Co-Fe-B/MgO nanomagnets with PMA, employing localized ion irradiation (not implantation), thus controlling domain-wall (DW) nucleation. Gallium ions are chosen, as they are known to reduce the anisotropy in crystalline multilayer systems effectively [12]. Heavier atoms, furthermore, can be stopped much more effectively, reducing potential damage to underlying layers. The dose-dependent irradiation effects are first evaluated at the film level, probing material parameter and domain configurations, before the focus is shifted toward the irradiation of nanostructures and time-domain measurements. We thereby explain the different time-dependent DW-nucleation probabilities, from which information regarding nucleation mechanisms (coherent rotation or depinning) and irradiation effects are derived. Unitizing this analysis, we employ irradiation at the centers of the magnets to control the switching fields and force DW nucleation via depinning instead of coherent rotation.

*simon.mendisch@tum.de
†fabrizio.riente@polito.it

 © 2021 American Physical Society

II. FABRICATION AND CHARACTERIZATION

A. Device fabrication

The magnetic thin film analyzed in this work is based on a Ta/Co-Fe-B/MgO/Ta sandwich structure with a $Co_{20}Fe_{60}B_{20}$ alloy target and a nominal thicknesses of $Ta_2/CoFeB_1/MgO_2/Ta_3$ (values given in nanometers). The film is deposited at room temperature via confocal rf-magnetron sputtering (base pressure $< 2 \times 10^{-7}$ mbar) onto silicon ⟨100⟩ substrates, topped by a thermal oxide (thickness approximately 50 nm). The individual materials are deposited at a constant working pressure of 4 μbar (approximately 3 mTorr) with MgO as an exception (<1 μbar). The target power density is 0.5 W cm^{-2} for all materials. Postdeposition annealing (250°C, N_2 atmosphere) is used to set the effective anisotropy to the desired value of approximately 1.3×10^5 J m^{-3}. The stack is subsequently structured via focused-ion-beam (FIB) lithography (using PMMA as a positive ion-beam resist) to realize the designed test structures. The lithography profile is inverted, after PMMA development, by depositing a 5-nm-thick Ti hard mask and removing the residual PMMA in a lift-off process. Finally, the nonmasked areas are physically etched via Ar^+ ion-beam etching ($E = 350$ eV). To generate ultrashort magnetic field pulses, on-chip field coils are placed around the structures via conventional optical contact lithography together with the deposition of a Cu metal layer (approximately 750 nm) and a second lift-off process. The Ga^+ ion irradiation, which changes the magnetic properties, is carried out using a 50-keV FIB microscope (Micrion 9500ex) with a spatial resolution (beam diameter) of approximately 10 nm. For large areas, the beam is defocused to achieve homogeneous irradiation results.

B. Magneto-optical imaging

The magnetic films and nanostructures are characterized via Wide-field Kerr microscopy (WMOKE), both for the quasistatic case as well as for the time-domain measurements. Static coercivities are obtained by merely applying a staircase field profile with images taken at every step. In a later data-processing step, the coercivities of the individual magnets can be derived from the respective brightness changes in the images. Reliable time-domain measurements, however, require a more sophisticated measurement scheme. Ultrashort magnetic field pulses are generated via (single winding) on-chip coils, which are bonded to pulse-discharge capacitors on the high side and a low-side switch. This switch is driven by a fast gate driver and is addressed with an Agilent 81111A Pulse Generator (for a more detailed description of the on-chip field generation scheme, see the Supplemental Material [13]). To measure the nucleation probability p_{nuc} of the individual magnets at short time scales, the on-chip field pulses in the nanosecond range are synchronized with the image acquisition of a high-dynamic-range sCMOS camera. Figure 1 depicts a rough sketch of this imaging procedure. After the initial saturation of the magnets, a first reference image is taken. Subsequently, the on-chip pulse is triggered to nucleate a DW. A second propagation pulse with a low amplitude (approximately 3 mT) is generated thereafter via an external electromagnet to ensure the complete magnetization reversal (and thus optical detection) upon the nucleation of a DW. The second image, taken after the pulses, enables differential imaging in a later data-processing step. This procedure is repeated multiple times to retrieve the nucleation probability at a given field amplitude and pulse width. Examples of the probability evolution are displayed in Fig. 3(a). The advantage of this procedure, compared to laser-based approaches, is the ability to probe large numbers of magnets simultaneously by facilitating image recognition to detect and label all magnets within the image frame.

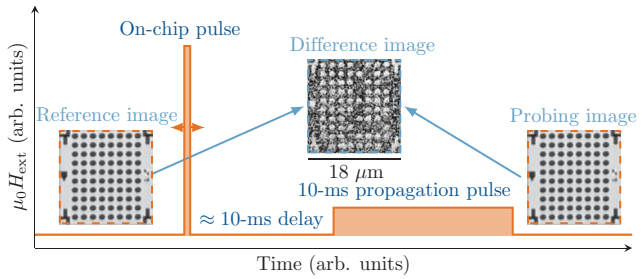

FIG. 1. A sketch of the employed measurement scheme, illustrating the procedures in a timeline. First, a reference image of the saturated magnet array is taken. Subsequently, the on-chip pulse with varying widths of $t_p = 20$ ns to 100 μs is triggered, before a second millisecond-long pulse is used to propagate the remaining DWs and complete the reversal process. After the propagation pulse, a second image is taken, which is subtracted from the reference image. The final difference image is then used for the later analysis. This procedure is repeated multiple times to gain statistical data for the magnets in the image frame.

III. RESULTS AND DISCUSSION

A. Areal irradiation and static measurements

To understand and interpret the irradiation-dependent changes in the DW dynamics of nanostructures, we first analyze the irradiation effects at the film level. This allows probing of the essential material parameter (M_s and K_{eff}) via comparatively simple, though error-prone, magnetometer measurements. The material parameters are extracted from superconducting quantum interference device (SQUID) and vibrating sample magnetometer (VSM) measurements. K_{eff} is thereby approximated from the hard-axis loops via the area method [14]. The uniaxial anisotropy constant K_u, necessary for the micromagnetic simulations, is calculated as $K_u = K_{\mathrm{eff}} + (1/2)\mu_0 M_s^2$. Figure 2(a) depicts the irradiation-induced changes in M_s

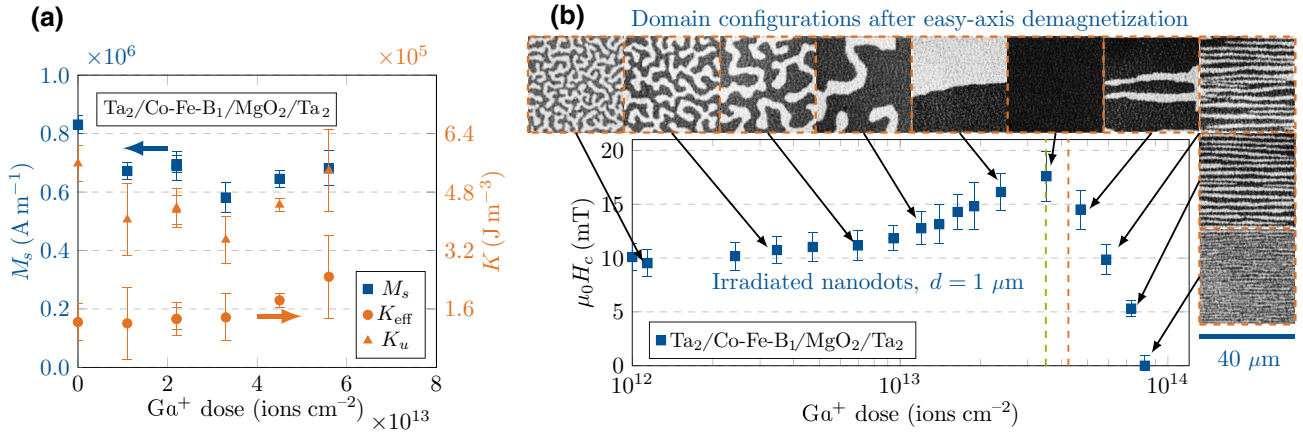

FIG. 2. (a) A plot of the measured material parameter M_s and K_{eff} of the film, together with the calculated uniaxial anisotropy term $K_u = K_{\text{eff}} - \frac{1}{2}\mu_0 M_s^2$ versus the applied ion dose. (b) The Ga^+ dose-dependent coercivity evolution of circular $Ta_2/CoFeB_1/MgO_2$ nanomagnets ($d = 1$ μm). The error bars indicate the raw FWHM switching-field distribution of 80 magnets each (for the respective histograms, see the Supplemental Material [13]). The surrounding domain images display dose-correlated domain patterns imaged on the same film after irradiation and easy-axis demagnetization (via a damped oscillation field). The colored dashed lines serve as markers, indicating doses used in a more detailed analysis.

as well as K_{eff} with increasing ion dose, determined from the magnetometer data. Similar to reports on the He^+ irradiation of Ta/Co-Fe-B/MgO films, a decrease in saturation magnetization accompanied by an increase in effective anisotropy is observed [9,10]. Figure 2(b), on the other hand, depicts the irradiation-dependent static coercivities (H_c) of circular nanodots ($d = 1$ μm) and respective (dose-matched) domain images of irradiated films. The changes in the coercivities and domain sizes enable a more detailed though qualitative assessment of the shifts in the anisotropy landscape, as both are closely related to K_{eff}. At small film thicknesses, the domain size (W_{domain}) can be approximated by $W_{\text{domain}} \approx t_{\text{film}} e^{\pi D_0/t_{\text{film}}}$ [where the dipolar lengths $D_0 = (\pi\sqrt{A_{\text{ex}}K_{\text{eff}}}/\mu_0 M_s^2)$] [15,16]. The data points in Fig. 2(b) display the center of the respective switching-field distribution (SFD), with the error bars indicating the full width at half maximum (FWHM). Thereby, 80 magnets are probed for each ion dose. The magnets are placed 1 μm apart to inhibit any relevant dipolar interaction between the magnets from obscuring the measurements. The coercivities and domain sizes initially increase for low and medium doses but start to fall off at doses higher than approximately 3.5×10^{13} ions cm^{-2}, with the domain size dropping below the resolution limit at a dose of approximately 8×10^{13} ions cm^{-2}. The magnets also cross the single-domain threshold near this point. While the reduced coercivities could potentially be the result of an increased defect density (this would, however, not explain the initial increase in H_c), the shrinking domain sizes strongly indicate a loss of the perpendicular magnetic anisotropy, which leads to reduced coercivities. The decrease in both the domain sizes and coercivities strongly indicates a degradation of the PMA starting at doses $> 3.5 \times 10^{13}$ ions cm^{-2}. It has to be noted that the apparent decrease in K_{eff} above approximately 3.5×10^{13} ions cm^{-2} cannot be replicated via the corresponding magnetometer measurements. This fact might, however, be explained by the macroscopic nature of the magnetometer measurements, complicating the detection of small changes in the anisotropy landscape. It is difficult to explain the nonmonotonic evolution of K_{eff} without a detailed stoichiometric analysis and therefore no comprehensive explanation can be given. However, as with He^+ irradiation [9,17], the behavior might be explained by the respective atomic weights of the different elements inside the stack, giving the Ga^+ ions a much larger probability of interacting with the heavy Ta rather than with the comparatively light Fe, Co, or O atoms. Since tantalum is known for its large magnetic dead layer in contact with ferromagnets, we assume intermixing at the Ta/Co-Fe-B interface to be the dominant cause of the decrease in M_s [9,17]. A possible explanation for the nonmonotonicity in K_{eff} could be that due to this reduced interaction probability, the damage to the Co-Fe-B/MgO interface and thus K_u only becomes relevant at much higher doses [9,17]. Closely related to this is the likely accumulation of tantalum atoms at the Co-Fe-B/MgO interface, which also strongly affects the anisotropy [18]. An interesting observation related to the anisotropy decrease is the formation of highly ordered stripe domains at high ion doses, indicating changes in more then the primary material parameter. This is in line with reports on the increase of the interfacial Dzyaloshinskii-Moriya interaction upon the irradiation of Ta/Co-Fe-B/MgO films [11].

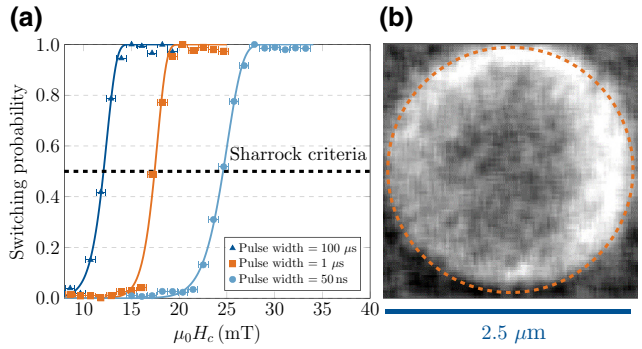

FIG. 3. (a) The measured field-dependent nucleation probabilities of a 1-μm nanomagnet for different pulse widths. (b) The 1000 superimposed differential WMOKE images of the nucleation events inside a 2.5-μm-wide nanodot. The areas of increased brightness indicate higher nucleation probabilities. Nucleation is achieved using 20-ns-long pulses without consecutive propagation pulses.

B. Controlling the magnetization reversal

We have already shown that the coercivities of the magnets can be effectively tailored by adjusting the ion dose. However, static measurements only provide limited insight into the reversal mechanisms and are not suited to derive relevant conclusions. Therefore, we attempt a characterization of the irradiation-dependent reversal process by probing the time-dependent magnetization reversal. For this purpose, we provide a sample base of at least 40 magnets per data point, reducing the effects of statistical outliers. Contrary to the distribution of the demagnetizing fields, DWs in Co-Fe-B/MgO nanomagnets usually nucleate at the edges of the nanostructures due to an etch-damage-induced lowering of K_{eff} [19,20]. To validate this assumption for the test structures, 20-ns-long magnetic field pulses are used to nucleate DWs in circular nanodisks with a diameter of 2.5 μm, with the goal of locating the nucleation sights via repeated differential WMOKE imaging. Figure 3(b) displays the combined differential WMOKE image of ten different disks with a total of 1000 superimposed images to qualitatively show the local nucleation probability. The bright areas thereby indicate an increased DW-nucleation probability. The image indicates the accumulation of nucleation events at the edges of the disks, while an inhomogeneity in the applied on-chip fields most likely explains the asymmetry toward the right side (for images of single nucleation events and a sanity check without DW nucleation, see the Supplemental Material [13]). The conformation of nucleation from the edges has severe implications. Instinctively, one would expect the nucleation to occur at points with strong demagnetizing fields, i.e., the center of the magnet. However, the demagnetizing fields are lowest at the edges, leading to the conclusion that the reduction in K_{eff} must be significantly larger than the anisotropy variations in the centers of the magnets. Furthermore, the question arises as to whether the DW nucleation occurs via coherent rotation according to the *Stoner-Wohlfarth* (SW) model or by depinning from an area with easy-plane anisotropy [21,22]. This can be resolved by considering the time evolution of both processes. The rotation fields scale over time according to the well-established *Sharrock* formalism based on an Arrhenius switching model of a SW particle and can be expressed by

$$H_{\mathrm{nuc}} = H_{s0}\left\{1 - \left[\frac{k_B T}{E_0}\ln\left(\frac{f_0 t_p}{\ln(2)}\right)\right]^{\frac{1}{2}}\right\}, \qquad (1)$$

where H_{s0} is the switching field at 0 K, f_0 is the attempt frequency (approximately 1×10^9 Hz), and E_0 is the energy barrier without an applied field [21,23,24]. In contrast, the time necessary for a DW to overcome the anisotropy gradient and depin can be derived from the related Néel-Brown theory and scales according to

$$\tau = f_0^{-1}\exp\left[\frac{M_s V_a}{k_B T}(H_d - H)\right], \qquad (2)$$

where V_a is the activation volume and H_d is the depinning field at 0 K [22,25,26]. By characterizing the switching fields over a wide range of different time scales (pulse widths) and comparing the evolution to the models in Eqs. (1) and (2), it is possible to gather detailed information about the switching mechanisms. Figure 4 displays the pulse-width-dependent nucleation fields of the circular nanodots with a diameter of 1 μm. The measurements cover time scales ranging from the quasistatic case down to 20 ns. The data points resemble the center of the distribution, with the error bars again displaying the FWHM. The nucleation field H_{nuc} is furthermore defined according to Eq. (1), as the field with a switching probability $p_{\mathrm{nuc}} \geq 50\%$. Figure 3(a) shows a series of exemplary nucleation-probability measurements for different pulse widths, with the switching criteria indicated as a dashed line. The plot furthermore depicts corresponding fits according to the Arrhenius switching model with the probability $p_{\mathrm{nuc}} = 1 - \exp(-t_p/\tau_{\mathrm{nuc}})$, with τ_{nuc} as the inverse of the nucleation rate [24].

1. Nucleation by coherent rotation

We first consider the pristine magnets and compare the data to the aforementioned nucleation and depinning dominated models. The nucleation fields show good agreement with the numerical fits according to Eq. (1), displayed as black lines; the fitting parameters converge to $H_{s0} = (36.83 \pm 1.65)$ mT and $(E_0/k_B T) = (30.98 \pm 2.9)$. Additionally, we attempt to fit Eq. (2) analytically by minimizing its cumulative error function, utilizing a linearized least-squares problem (for a detailed description of the

used mathematical model use, see the Supplemental Material [13]). However, an acceptable solution (displayed as a dotted line) is only obtained excluding pulse widths $< 1\ \mu$s, thus arguing against depinning as the primary DW-nucleation mechanism, at least for very short time scales. Interestingly, however, at long time scales ($> 10\ \mu$s), depinning from the nucleation sites could very well be the limiting factor, thus explaining the apparent underestimation of the *Sharrock* fits at quasistatic fields. The question now arises whether Ga^+ irradiation not only increases the effective anisotropy of the core of the disk but whether its effect on the predamaged edges is different. Therefore, Fig. 4 also displays the time evolution of nanodisks homogeneously irradiated with a dose of 3.5×10^{13} ions cm^{-2} and 4.3×10^{13} ions cm^{-2}. The doses are chosen to probe the peak of the static coercivity increase as well as a position within the downward slope. For better illustration, the doses are marked, in their respective colors, as dashed lines in Fig. 2(b). The slopes again indicate nucleation by coherent rotation as the dominant mechanism. From the corresponding fits, we derive the energy barriers to be $(E_0/k_BT) = (34.42 \pm 2.1)$ and $(E_0/k_BT) = (27.57 \pm 1.8)$, respectively. The fields at which these barriers become zero are determined to be $H_{s0} = (87.67 \pm 2.40)$ mT and $H_{s0} = (76.01 \pm 2.90)$ mT. The energy barrier can be roughly modeled as $E_0 \approx K_{\text{eff}}^{\text{nuc}} V_{\text{nuc}}$, where V_{nuc} is the nucleation volume and $K_{\text{eff}}^{\text{nuc}}$ is the anisotropy of the rotating volume or grain [23]. The nucleation field at 0 K, on the other hand, is equal to the anisotropy field $H_{\text{anis}} \approx 2K_{\text{eff}}^{\text{nuc}}/M_s$ [21,23]. The assumption of M_s values comparable to those measured for similar ion doses on films allows approximation of the effective anisotropy and the critical size of the volume starting the magnetization reversal. Table I displays the calculated values for $K_{\text{eff}}^{\text{nuc}}$ and V_{nuc} assuming a constant saturation magnetization of approximately 6.5×10^5 A m^{-1} for the irradiated magnets. The calculated effective anisotropies of the critical volumes are roughly one order of magnitude smaller than the values obtained for the respective films. Furthermore, the irradiation-induced changes in $K_{\text{eff}}^{\text{nuc}}$ and H_{s0} agree well with the in Fig. 2(b) displayed evolution in coercivities and domain sizes. Next to K_{eff}, it is also possible to approximate the uniaxial anisotropy components K_u of the nucleation sites and their evolution ($K_u = K_{\text{eff}} + (1/2)\mu_0 M_s^2$). While for the pristine magnets, K_u amounts to approximately 4.4×10^5 J m^{-3}, it drops to approximately 3×10^5 J m^{-3} and approximately 2.9×10^5 J m^{-3} for the irradiated magnets. This strengthens the argument for a simultaneous decrease in M_s and K_u, still leading to a combined increase in K_{eff}. Defects introduced during irradiation cannot explain the measured increase in $K_{\text{eff}}^{\text{nuc}}$. The nucleation volumes, on the other hand, seemingly decrease upon irradiation, thus partially mitigating the effects of the increasing anisotropy on the nucleation fields. The assumption of a square-shaped volume allows the assignment of a characteristic length l_{nuc} to the effective nucleation area ($l_{\text{nuc}} = \sqrt{V_{\text{nuc}}/(t_{\text{film}})}$). In the case of the pristine magnets, this results in a length of approximately 92 nm, which reduces to 71 nm and 68 nm for the irradiated magnets, respectively. These sizes are interesting, as they are significantly larger than the often associated grain sizes, which in the case of the quasiamorphous Ta/Co-Fe-B/MgO film should range around approximately 10 nm [20,27]. A lower limit for the nucleation volumes will, however, be imposed by the DW widths Δ_{DW}, as the area of the nucleated volume must at least support one DW ($V_{\text{nuc}} \approx \Delta_{\text{DW}}^2 \cdot t_{\text{film}}$, $l_{\text{nuc}} \approx \Delta_{\text{DW}}$) [28]. The DW widths can be approximated from the anisotropy, via the relation $\Delta_{\text{DW}} \approx \pi\sqrt{A_{\text{ex}}/K_{\text{eff}}}$, where A_{ex}, the exchange stiffness, is assumed to be 2×10^{-11} J m^{-2} for Co-Fe-B [29]. Within the frame of the coherent rotation model, the nucleating particle has a constant anisotropy ($K_{\text{eff}}^{\text{nuc}}$), which would result in a DW width of approximately 110 nm for the pristine magnets and reduced widths of approximately 83 nm and approximately 89 nm for the irradiated magnets. These values are in good agreement with those obtained for the nucleation lengths. This picture, however, might

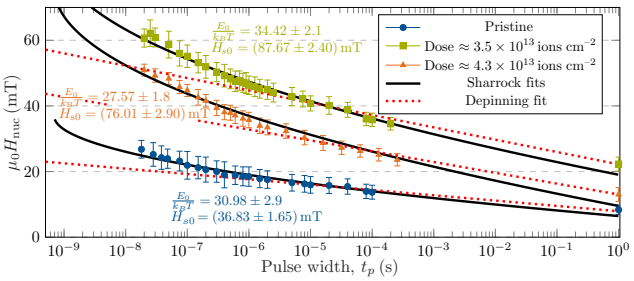

FIG. 4. The calculated nucleation fields (H_{nuc}) depending on the applied pulse width. The individual data points display the centers of the SFDs, with the error bars displaying the FWHM. The corresponding *Sharrock* fits are illustrated as black lines. A fit, assuming depinning-mediated nucleation according to Eq. (2) for the pristine magnets, is illustrated in red.

TABLE I. The saturation magnetization M_s, the anisotropy of the nucleation volume $K_{\text{eff}}^{\text{nuc}}$, and the nucleation volume V_{nuc}, calculated from the respective fits of pristine and irradiated magnets.

Dose (ions cm^{-2})	M_s (A m^{-1})	$K_{\text{eff}}^{\text{nuc}}$ (J m^{-3})[a]	V_{nuc} (m^3)[a]
Pristine	8.3×10^5[b]	1.5×10^4	8.4×10^{-24}
3.5×10^{13}	$\approx 6.5 \times 10^5$[c]	$\approx 2.9 \times 10^4$	$\approx 5.0 \times 10^{-24}$
4.3×10^{13}	$\approx 6.5 \times 10^5$[c]	$\approx 2.5 \times 10^4$	$\approx 4.6 \times 10^{-24}$

[a] $K_{\text{eff}}^{\text{nuc}} \approx 1/2 H_{s0} M_s$, $V_{\text{nuc}} \approx E_0/K_{\text{eff}}^{\text{nuc}}$.
[b] Data taken from Fig. 2(a).
[c] Approximated from the magnetometer measurements in Fig. 2(a).

be too simplistic to describe the anisotropy landscape at the edges accurately, where the DW nucleations are most likely to originate. Attempts to directly observe the position of DW nucleation as for the pristine magnets are not successful, as the higher nucleation fields result in very high DW velocities, leading to complete reversals already within a few nanoseconds. The etch damage during patterning will induce an anisotropy drop along a gradient of typically 10–20 nm [20]. On the other hand, even inside the undamaged magnets, Δ_{DW} will only decrease to values around approximately 40 nm (using the anisotropies measured on films). Therefore, the obtained nucleation lengths would only be off by a factor of 2 or less when considering the added influence of the edge damage. This is a reasonable result, especially when factoring in all the mentioned uncertainties.

2. Nucleation by depinning

Control of the position of DW nucleation with high spatial accuracy is an essential requirement for prospective DW applications. By targeted irradiation, the anisotropy can, in principle, be lowered locally, creating the so-called ANCs [30]. However, the known occurrence of significant anisotropy lowering (with unknown distribution) toward the edges severely impedes efforts to create the nucleation volume with the lowest PMA reliably. Nucleation by DW depinning from a fixed anisotropy gradient [e.g., an area with strongly reduced or easy-plane (negative) anisotropy], however, offers an interesting alternative. Here, the anisotropy can be lowered by much larger extents, provided that the depinning fields fall below the intrinsic nucleation fields (via coherent rotation) [12]. Furthermore, the depinning process is governed by different time dynamics, leading to potentially lower switching fields upon approaching time scales close to τ_0, which are, of course, most interesting for applications. For this purpose, ANCs with an anisotropy close to zero are placed in the center of the nanomagnet ($d = 1$ μm), employing a double-irradiation approach. First, a homogeneous background irradiation with a dose of 4.25×10^{13} ions cm^{-2} is used to increase K_{eff} beyond its peak (at approximately 3.5×10^{13} ions cm^{-2}). The effective anisotropy is subsequently reduced by a second target irradiation in the center, with an additional 3.8×10^{13} ions cm^{-2} leading to a cumulative total dose of approximately 8×10^{13} ions cm^{-2} for the ANC. For this dose, Fig. 2(b) shows a coercivity of approximately 0 mT, with the magnetization effectively following the external field. The ANC position and the magnetization direction in remanence are observed by differential WMOKE imaging of larger 2.5-μm-wide magnets, as displayed in Fig. 5(a). The bright spot ($d \approx 400$ nm) at the center of the circular magnet, which matches the size of the irradiated ANC area, indicates a change in the magnetization direction and thus the presence of a DW between the ANC and the magnet. However, it is not clear whether the magnetization of the ANC points in-plane or whether it is being aligned antiparallel by the demagnetizing fields of the host magnet. Complementary to the experiments, a simulation model with an in-plane ANC is developed to better analyze and understand the magnetization reversal in this geometry. The model parameters are chosen to best approximate the characterized magnets. A detailed representation is depicted in Figs. 5(b) and 5(c). The depinning mediated magnetization reversal, starting from the DW surrounding the ANC, is analyzed by again measuring the time dependence of the switching fields. This is done for a series of magnets with centered circular ANCs (diameters ranging from $d = 100$ nm to $d = 400$ nm). The cumulative ion dose of all the ANCs is 8×10^{13} ions cm^{-2} (keeping in mind the background dose of 4.25×10^{13} ions cm^{-2}). Figure 6 depicts the measured nucleation fields with their corresponding fits according to Eq. (2). The measured nucleation fields appear to agree well with the depinning model down to low-microsecond time scales. From this point onward, H_{nuc} seemingly increases drastically, reaching levels close to those of the irradiated magnets in Fig. 4. However, a doubling of the nucleation fields within one order of magnitude (time) is hardly explainable by any reasonable depinning or rotation model. To explain the observed increase in H_{nuc}, it is necessary to consider the measurement procedure discussed in Sec. II B. After the initial (nanosecond-long) nucleation pulse, a secondary (millisecond-long) low-field pulse is used to propagate the DW and ensure a complete

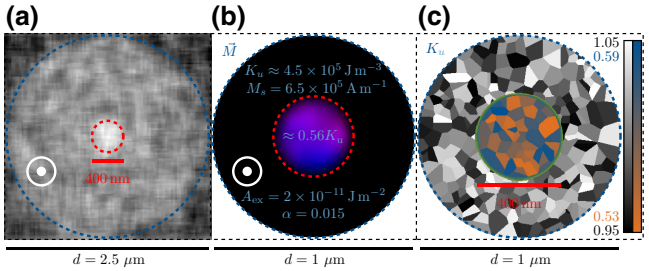

FIG. 5. (a) A differential WMOKE image of a Ta/Co-Fe-B/MgO nanodisk with a diameter of 2.5 μm. The image displays the remanent magnetization at 0 mT after saturation with 10 mT. The ANC, with a diameter of approximately 400 nm, is visible at the center, with its magnetization seemingly pointing opposite to the remaining magnet. (b) The domain configuration of the respective MuMax3 model with a diameter of 1 μm in remanence. The material parameters are depicted, with special notice given to K_u inside the ANC area. (c) The grain structure of one of the simulated samples, with the colors representing the respective anisotropies. The ANC and the magnet are separated by a 30-nm broad transition region (illustrated in green) with a linear anisotropy gradient. The simulated grain and mesh sizes of the dots are set to approximately 15 nm and 2.5 × 2.5 nm, respectively. The simulation parameters are taken from measurements, except for α and A_{ex}, which are taken from the literature [29].

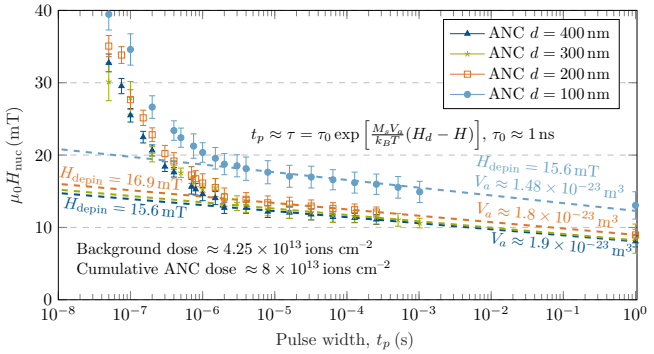

FIG. 6. The measured nucleation fields of double-irradiated nanodisks ($d = 1$ μm) as a function of the applied pulse width t_p. The disks feature circular different-sized ANCs at their centers, with the respective diameters given in the legend.

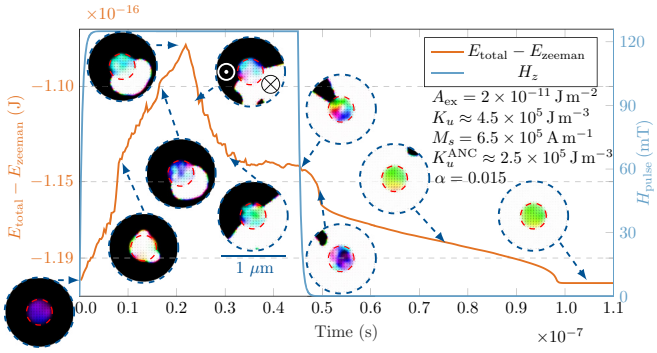

FIG. 7. A plot of the simulated magnetization-reversal process, depicting a 1-μm circular nanomagnet with a centered ANC ($d = 400$ nm). The graph displays the combined magnetic energies (excluding the *Zeeman* term) in combination with snapshots of the domain structure at relevant points. The assumed material parameters are listed in the plot (for further information about the simulations, see the Supplemental Material [13]).

magnetization reversal. However, the time between these two pulses allows the magnetization to relax back into the nearest local energy minimum. For a significant portion of the reversal process, this means to flip back into the initial state. We attempt to explain this phenomenon by a simplified but vivid model and underline it via micromagnetic simulations and related measurements. After the initial depinning from the ANC, the domain expansion can, to a first approximation, be modeled as the expansion of a circular bubble from the point of depinning (engulfing half of the ANC area to reduce its DW length). During this process, the system gains exchange and anisotropy energy as the DW length grows with the circumference ($\propto 2\pi r_{\mathrm{domain}}$) until reaching the edge of the magnet, where it splits into two DWs with lengths $\propto r_{\mathrm{magent}}$. The reducing demagnetizing fields do not compensate for this energy gain, as the magnet features a single-domain ground state. Without an external field, the bubble—provided that it has not reached the edge—tends to collapse (it snaps back to the starting point) as the DW tries to lose energy by reducing its length. This effective force on the DW is also described as a Laplace-like pressure, reported in circular domain structures, with a $(1/r)$ dependence [20,31,32]. Figure 7 illustrates the evolution of the total energy (without *Zeeman* terms) and respective snapshots of the domain structure throughout the reversal process. The data and images are derived from MuMax3 micromagnetic simulations of a 1-μm nanomagnet with a centered ANC according to Figs. 5(b) and 5(c) [33]. The simulation parameters (listed in the plot) are thereby taken from measurements when possible to resemble the characterized magnets best and α is taken from the literature [29]. As described in the above model, the total energy initially increases significantly as the bubble domain expands toward the edge, where it reaches a tipping point before falling off, as the DW splits, reducing its length. After overcoming this energy barrier, the domain configuration can be described as quasistable until the propagation pulse completes the reversal process.

In other words, Fig. 6 displays the fields necessary to form a quasistable domain rather than to depin a DW. In addition to dynamic simulations, it is possible to test the model implicitly by measuring certain dependencies. Assuming the correctness of the model, larger magnets would require stronger fields to propagate the DW to the edge within the pulse duration. Figure 8 compares the nucleation fields of two different magnet sizes with diameters of 1 μm and 2.5 μm. For pulse widths $t_p < 200$ ns, the measured nucleation fields start to diverge, with the larger magnets requiring significantly higher field strengths for the DWs to form the necessary quasistable multidomain state. However, it has to be noted that data for the 2.5-μm magnets are only available for three samples, compared to the 40 for the 1-μm magnets. Besides the dimensional scaling, it is also worth considering the time scales of possible bubble collapses. Although it is not directly possible to observe this process via WMOKE imaging, information about the time scales on which these collapses occur can nevertheless be inferred using consecutive on-chip field pulses with varying pulse periods (dead times between pulses). Using a fixed pulse width of 50 ns but sweeping the time between the pulses and measuring the effects on the nucleation fields, it is possible to derive upper and lower bounds for the collapse times. If the domain collapses within the time between pulses, the switching fields should be independent of the number of pulses (at least in the first approximation, not considering the higher attempt count per measurement).

Starting at approximately 1 μs, a clear reduction in the measured nucleation fields is observed. At pulse periods of 200 ns (150 ns dead time), however, the measured fields are still twice as high as expected for the cumulative pulse duration of 1 μs. Only for dead times < 50 ns are comparable nucleation fields observed. As a sanity check,

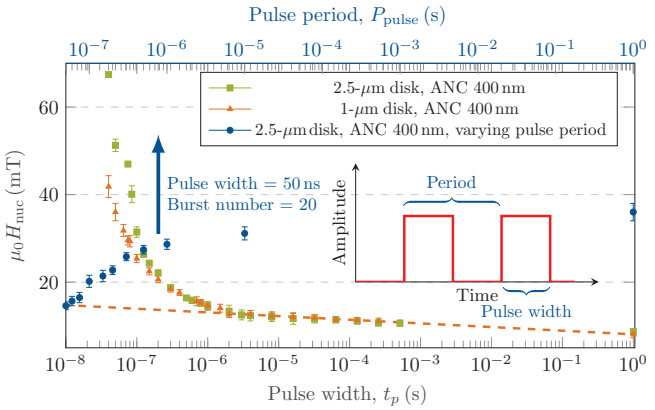

FIG. 8. The combined plot shows, on the lower x axis, the nucleation fields over different pulse widths, 1-μm (orange) and 2.5-μm (green) nanodisks. The second plot, associated with the upper x axis (blue), displays a sweep of the pulse period P_{pulse} and its effects on the measured nucleation fields. The cumulative pulse width is thereby kept constant at 1 μs (Burst# $= \frac{1\ \mu\text{s}}{50\ \text{ns}}$).

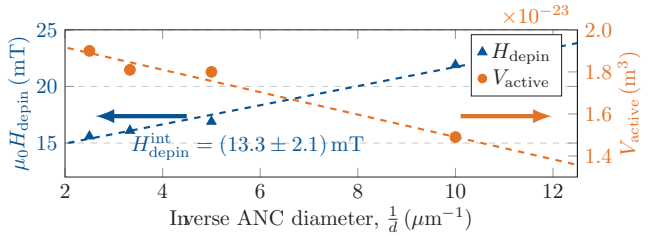

FIG. 9. A plot of the depinning fields H_{depin} at 0 K (on the left) combined with the activation volume V_a (right) for the depinning from a circular ANC, depending on the ANC curvature $\frac{1}{d_{\text{ANC}}}$. Both exhibit a linear $\frac{1}{d}$ dependence with, however, complementary slopes. The dashed lines depict the best linear fits.

we again consider the *Stoner-Wohlfarth*-particle-based rotation model (for a detailed discussion, see the Supplemental Material [13]). However, the time-dependent nucleation probabilities via coherent rotation are independent of the magnet size and do not scale with the pulse period. All these observations and simulations let us assume that the depinning fields scale according to Eq. (2) even below microsecond pulse widths. Splitting the nucleation-field measurements (displayed in Fig. 6) at $t_p \approx 1$ μs would technically allow modeling of the two slopes separately via the *Sharrock* equation. However, the presence of a DW at the ANC edge [made evident by the WMOKE image in Fig. 5(a)] even after initial OOP saturation, plus the scaling of the nucleation fields with the ANC curvature and pulse period lead us to exclude this model. Upon analyzing the ANC-size-dependent depinning fields in Figs. 6 and 9, it becomes evident that the depinning process from the circular sources scales $\propto (1/d_{\text{ANC}})$ (the curvature of the circle) and thus is similar to DW depinning from a notch [34–36]. Figure 9 depicts both the effective activation volumes (V_a) and the depinning fields at 0 K versus $(1/d_{\text{ANC}})$. V_a (not to be confused with the nucleation volume V_{nuc} discussed earlier) is calculated from Eq. (2), assuming $M_s \approx 6.5 \times 10^5$ A m^{-1} [approximated from the magnetometer data in Fig. 2(a)]. The intrinsic depinning field $H_{\text{depin}}^{\text{int}}$ of the anisotropy gradient can be derived from the zero intercept of the linear fit to be $H_{\text{depin}}^{\text{int}} = (13.3 \pm 2.1)$ mT [34]. Analysis of the evolution of the activation volume is more complicated. First, it is necessary to point out that the calculated absolute values depend strongly on the value of M_s, which is not precisely known. The sizes for V_a, although showing a linear $(1/d_{\text{ANC}})$ dependence, shrink only marginally compared to the physical dimensions of the respective ANCs. To illustrate this better, we translate the activation volume into an effective ANC diameter $d_{\text{ANC}}^{\text{eff}}$, assuming a cylindrical-shaped volume ($d_{\text{ANC}}^{\text{eff}} = 2\sqrt{V_a/(\pi t_{\text{film}})}$). This yields effective diameters from approximately 140 nm to 160 nm, indicating that, especially for the larger ANCs, only a small portion takes part in the depinning process. This complies with the depinning models, predicting depinning at the area with the lowest anisotropy gradient.

IV. CONCLUSION

Ta/Co-Fe-B/MgO films and nanostructures are irradiated with Ga^+ ions to globally and locally modify the magnetic energy landscape, aiming to control the position of DW nucleation effectively. It is shown that K_{eff} initially increases up to doses of 3.5×10^{13} ions cm^{-2}, followed by a steep decline, crossing the easy-plane threshold at approximately 8×10^{13} ions cm^{-2}. The time-dependent nucleation-field analysis of pristine and irradiated magnets determines the anisotropies of the nucleation volumes to be roughly one order of magnitude smaller than the values obtained from film-level magnetometer measurements. Control over nucleation points and fields is achieved, employing a second focused irradiation, creating artificial regions with easy-plane magnetization, from which a DW can depin. The fields needed to depin a DW from this anisotropy gradient scale $\propto (1/d_{\text{ANC}})$.

ACKNOWLEDGMENTS

We would like to thank Michael Wack for the support in the VSM measurements. Furthermore, we would like to thank the Technical University of Munich (TUM) International Graduate School of Science and Engineering (IGSSE) for its financial support. We gratefully acknowledge the support of the NVIDIA Corporation with the donation of a Titan XP GPU, which was used for this research. Finally, we would like to acknowledge the support of the Central Electronics and Information Technology Laboratory—ZEIT$^{\text{lab}}$.

[1] K. Garello, F. Yasin, S. Couet, L. Souriau, J. Swerts, S. Rao, S. Van Beek, W. Kim, E. Liu, S. Kundu *et al.*, in *IEEE Symposium on VLSI Circuits* (IEEE, 2018), p. 81.

[2] F. Riente, S. Mendisch, L. Gnoli, V. Ahrens, M. R. Roch, and M. Becherer, Ta/CoFeB/MgO analysis for low power nanomagnetic devices, AIP Adv. **10**, 125229 (2020).

[3] K. Garello, F. Yasin, H. Hody, S. Couet, L. Souriau, S. Sharifi, J. Swerts, R. Carpenter, S. Rao, W. Kim *et al.*, in *Symposium on VLSI Circuits* (IEEE, 2019), p. T194.

[4] S. Sakhare, M. Perumkunnil, T. H. Bao, S. Rao, W. Kim, D. Crotti, F. Yasin, S. Couet, J. Swerts, S. Kundu *et al.*, in *IEEE International Electron Devices Meeting (IEDM)* (IEEE, 2018), p. 18.

[5] F. Xie, R. Weiss, and R. Weigel, Hysteresis compensation based on controlled current pulses for magnetoresistive sensors, IEEE Trans. Ind. Electron. **62**, 7804 (2015).

[6] M. Manfrini, A. Vaysset, D. Wan, E. Raymenants, J. Swerts, S. Rao, O. Zografos, L. Souriau, K. B. Gavan, N. Rassoul *et al.*, Interconnected magnetic tunnel junctions for spin-logic applications, AIP Adv. **8**, 055921 (2018).

[7] S. Mendisch, V. Ahrens, M. Kiechle, A. Papp, and M. Becherer, Perpendicular nanomagnetic logic based on low anisotropy Co/Ni multilayer, J. Magn. Magn. Mater. **510**, 166626 (2020).

[8] J. Fassbender and J. McCord, Magnetic patterning by means of ion irradiation and implantation, J. Magn. Magn. Mater. **320**, 579 (2008).

[9] T. Devolder, I. Barisic, S. Eimer, K. Garcia, J.-P. Adam, B. Ockert, and D. Ravelosona, Irradiation-induced tailoring of the magnetism of CoFeB/MgO ultrathin films, J. Appl. Phys. **113**, 203912 (2013).

[10] L. Herrera Diez, F. García-Sánchez, J.-P. Adam, T. Devolder, S. Eimer, M. El Hadri, A. Lamperti, R. Mantovan, B. Ocker, and D. Ravelosona, Controlling magnetic domain wall motion in the creep regime in He^+-irradiated CoFeB/MgO films with perpendicular anisotropy, Appl. Phys. Lett. **107**, 032401 (2015).

[11] L. H. Diez, M. Voto, A. Casiraghi, M. Belmeguenai, Y. Roussigné, G. Durin, A. Lamperti, R. Mantovan, V. Sluka, V. Jeudy *et al.*, Enhancement of the Dzyaloshinskii-Moriya interaction and domain wall velocity through interface intermixing in Ta/CoFeB/MgO, Phys. Rev. B **99**, 054431 (2019).

[12] J. H. Franken, M. Hoeijmakers, R. Lavrijsen, and H. J. Swagten, Domain-wall pinning by local control of anisotropy in Pt/Co/Pt strips, J. Phys.: Condens. Matter **24**, 024216 (2011).

[13] See the Supplemental Material at http://link.aps.org/supplemental/10.1103/PhysRevApplied.16.014039 for additional details on the measurement procedures, complementary measurements, and simulation parameter.

[14] M. Johnson, P. Bloemen, F. Den Broeder, and J. De Vries, Magnetic anisotropy in metallic multilayers, Rep. Prog. Phys. **59**, 1409 (1996).

[15] B. Kaplan and G. Gehring, The domain structure in ultrathin magnetic films, J. Magn. Magn. Mater. **128**, 111 (1993).

[16] O. Hellwig, A. Berger, J. B. Kortright, and E. E. Fullerton, Domain structure and magnetization reversal of antiferromagnetically coupled perpendicular anisotropy films, J. Magn. Magn. Mater. **319**, 13 (2007).

[17] H. T. Nembach, E. Jué, K. Poetzger, J. Fassbender, T. J. Silva, and J. M. Shaw, Tuning of the Dzyaloshinskii-Moriya interaction by He^+ ion irradiation, arXiv:2008.06762 (2020).

[18] N. Miyakawa, D. Worledge, and K. Kita, Impact of Ta diffusion on the perpendicular magnetic anisotropy of Ta/CoFeB/MgO, IEEE Magn. Lett. **4**, 1000104 (2013).

[19] X. Zhang, N. Vernier, W. Zhao, L. Vila, and D. Ravelosona, Extrinsic pinning of magnetic domain walls in CoFeB-MgO nanowires with perpendicular anisotropy, AIP Adv. **8**, 056307 (2018).

[20] Y. Zhang, X. Zhang, N. Vernier, Z. Zhang, G. Agnus, J.-R. Coudevylle, X. Lin, Y. Zhang, Y.-G. Zhang, W. Zhao *et al.*, Domain-Wall Motion Driven by Laplace Pressure in Co- Fe- B/MgO Nanodots with Perpendicular Anisotropy, Phys. Rev. Appl. **9**, 064027 (2018).

[21] E. C. Stoner and E. Wohlfarth, A mechanism of magnetic hysteresis in heterogeneous alloys, Philos. Trans. R. Soc. London, Ser. A, Math. Phys. Sci. **240**, 599 (1948).

[22] S.-B. Choe, D.-H. Kim, K.-S. Ryu, H.-S. Lee, and S.-C. Shin, Direct observation of barkhausen effect in strip-patterned ferromagnetic Co/ Pd multilayer films, J. Appl. Phys. **99**, 103902 (2006).

[23] M. P. Sharrock, Measurement and interpretation of magnetic time effects in recording media, IEEE. Trans. Magn. **35**, 4414 (1999).

[24] W. Wernsdorfer, E. B. Orozco, K. Hasselbach, A. Benoit, B. Barbara, N. Demoncy, A. Loiseau, H. Pascard, and D. Mailly, Experimental Evidence of the Néel-Brown Model of Magnetization Reversal, Phys. Rev. Lett. **78**, 1791 (1997).

[25] W. F. Brown Jr, Thermal fluctuations of a single-domain particle, Phys. Rev. **130**, 1677 (1963).

[26] L. Néel, Théorie du traînage magnétique des ferromagnétiques en grains fins avec applications aux terres cuites, Ann. géophys. **5**, 99 (1949).

[27] Y.-T. Chen and C. Chang, Effect of grain size on magnetic and nanomechanical properties of Co60Fe20B20 thin films, J. Alloys. Compd. **498**, 113 (2010).

[28] J. Vogel, J. Moritz, and O. Fruchart, Nucleation of magnetisation reversal, from nanoparticles to bulk materials, C. R. Phys. **7**, 977 (2006).

[29] R. Tomasello, E. Martinez, R. Zivieri, L. Torres, M. Carpentieri, and G. Finocchio, A strategy for the design of skyrmion racetrack memories, Sci. Rep. **4**, 6784 (2014).

[30] S. Breitkreutz, J. Kiermaier, S. Vijay Karthik, G. Csaba, D. Schmitt-Landsiedel, and M. Becherer, Controlled reversal of Co/Pt dots for nanomagnetic logic applications, J. Appl. Phys. **111**, 07A715 (2012).

[31] K.-W. Moon, J.-C. Lee, S.-G. Je, K.-S. Lee, K.-H. Shin, and S.-B. Choe, Long-range domain wall tension in Pt/Co/Pt films with perpendicular magnetic anisotropy, Appl. Phys. Express **4**, 043004 (2011).

[32] X. Zhang, N. Vernier, W. Zhao, H. Yu, L. Vila, Y. Zhang, and D. Ravelosona, Direct Observation of Domain-Wall Surface Tension by Deflating or Inflating a Magnetic Bubble, Phys. Rev. Appl. **9**, 024032 (2018).

[33] A. Vansteenkiste, J. Leliaert, M. Dvornik, M. Helsen, F. Garcia-Sanchez, and B. Van Waeyenberge, The design and verification of MuMax3, AIP Adv. **4**, 107133 (2014).

[34] K.-J. Kim, G.-H. Gim, J.-C. Lee, S.-M. Ahn, K.-S. Lee, Y. J. Cho, C.-W. Lee, S. Seo, K.-H. Shin, and S.-B. Choe, Depinning field at notches of ferromagnetic nanowires with perpendicular magnetic anisotropy, IEEE Trans. Magn. **45**, 4056 (2009).

[35] K.-J. Kim and S.-B. Choe, Analytic theory of wall configuration and depinning mechanism in magnetic nanostructure with perpendicular magnetic anisotropy, J. Magn. Magn. Mater. **321**, 2197 (2009).

[36] J. J. Goertz, G. Ziemys, I. Eichwald, M. Becherer, H. J. Swagten, and S. Breitkreutz-v. Gamm, Domain wall depinning from notches using combined in-and out-of-plane magnetic fields, AIP Adv. **6**, 056407 (2016).